HHS Public Access

Author manuscript

Neuroimage. Author manuscript; available in PMC 2021 September 29.

Published in final edited form as:

Neuroimage. 2021 August 15; 237: 118135. doi:10.1016/j.neuroimage.2021.118135.

A high-resolution interactive atlas of the human brainstem using magnetic resonance imaging

Syed M. Adil[a,b], **Evan Calabrese**[c], **Lefko T. Charalambous**[a,b], **James J. Cook**[b], **Shervin Rahimpour**[a], **Ahmet F. Atik**[d], **Gary P. Cofer**[b], **Beth A. Parente**[a], **G. Allan Johnson**[b], **Shivanand P. Lad**[a], **Leonard E. White**[e,f,*]

[a]Department of Neurosurgery, Duke University Medical Center, Durham, NC, United States

[b]Center for In Vivo Microscopy, Duke University Medical Center, Durham, NC, United States

[c]University of California San Francisco, Department of Radiology & Biomedical Imaging, San Francisco, CA, United States

[d]Department of Neurosurgery, Cleveland Clinic, Cleveland, OH, United States

[e]Department of Neurology, Duke University Medical Center, Durham, NC, United States

[f]Duke Institute for Brain Sciences, Duke University, Durham NC, United States

Abstract

Conventional atlases of the human brainstem are limited by the inflexible, sparsely-sampled, two-dimensional nature of histology, or the low spatial resolution of conventional magnetic resonance imaging (MRI). Postmortem high-resolution MRI circumvents the challenges associated with both

*Corresponding author at: Duke Institute for Brain Sciences, Duke University, Levine Science Research Center, Room M056, 308 Research Drive, Durham NC 27708. len.white@duke.edu (L.E. White).

Credit author statement

Syed Adil: Conceptualization, Methodology, Software, Formal analysis, Investigation, Data Curation, Writing – Original Draft, Writing – Review and Editing, Visualization

Evan Calabrese: Conceptualization, Methodology, Formal analysis, Writing – Original Draft, Writing – Review and Editing

Lefko Charalambous: Conceptualization, Methodology, Software, Formal analysis, Investigation, Data Curation, Writing – Review and Editing

James Cook: Methodology, Software, Formal analysis, Data Curation, Writing – Review and Editing, Visualization

Shervin Rahimpour: Conceptualization, Methodology, Formal analysis, Data Curation, Writing – Review and Editing

Ahmet Atik: Conceptualization, Writing – Review and Editing, Visualization

Gary Cofer: Methodology, Software, Formal analysis, Data Curation, Writing – Review and Editing, Visualization

Beth Parente: Conceptualization, Investigation, Writing – Review and Editing

G. Allan Johnson: Conceptualization, Methodology, Formal analysis, Data Curation, Resources, Writing – Original Draft, Writing – Review and Editing, Visualization, Supervision, Project administration, Funding acquisition

Shivanand Lad: Conceptualization, Resources, Writing – Review and Editing, Supervision, Project administration, Funding acquisition

Leonard White: Conceptualization, Methodology, Software, Formal analysis, Investigation, Data Curation, Writing – Original Draft, Writing – Review and Editing, Visualization, Supervision, Project administration

Declaration of Competing Interest

None

Data and code availability statement

As the primary purpose of this work is to provide a publicly available atlas, we are naturally sharing all of the images described in the manuscript. Please see Section 3.5 “Accessing the Atlas” for details on accessing the viewing platform. We are also happy to consider sharing raw data upon reasonable request (e.g. to undertake a new collaborative project).

Supplementary materials

Supplementary material associated with this article can be found, in the online version, at doi:10.1016/j.neuroimage.2021.118135.

modalities. A single human brainstem specimen extending from the rostral diencephalon through the caudal medulla was prepared for imaging after the brain was removed from a 65-year-old male within 24 h of death. The specimen was formalin-fixed for two weeks, then rehydrated and placed in a custom-made MRI compatible tube and immersed in liquid fluorocarbon. MRI was performed in a 7-Tesla scanner with 120 unique diffusion directions. Acquisition time for anatomic and diffusion images were 14 h and 208 h, respectively. Segmentation was performed manually. Deterministic fiber tractography was done using strategically chosen regions of interest and avoidance, with manual editing using expert knowledge of human neuroanatomy. Anatomic and diffusion images were rendered with isotropic resolutions of 50 μm and 200 μm, respectively. Ninety different structures were segmented and labeled, and 11 different fiber bundles were rendered with tractography. The complete atlas is available online for interactive use at https://www.civmvoxport.vm.duke.edu/voxbase/login.php?return_url=%2Fvoxbase%2F. This atlas presents multiple contrasting datasets and selected tract reconstruction with unprecedented resolution for MR imaging of the human brainstem. There are immediate applications in neuroanatomical education, with the potential to serve future applications for neuroanatomical research and enhanced neurosurgical planning through “safe” zones of entry into the human brainstem.

Keywords

Atlas; Magnetic resonance imaging; Diffusion tractography; Brainstem; Human brain

1. Introduction

In the quest to best visualize the human brain, there has traditionally been a trade-off between the high resolution of classical, analogue histology and the digital flexibility of modern magnetic resonance imaging (MRI). Contemporary histological techniques are labor-intensive, often requiring multiple specimens and/or sophisticated molecular-genetic enginnering in order to map different structures or tracts of anatomical interest with advanced imaging techniques such as 3D microscopy and CLARITY (Chung et al., 2013). The end product of conventional histology is typically sparse (serial sections with gaps between sections stained with the same probe) and/or anisotropic (with superior optical resolution in the plane of the histological section), with tissue destruction required for the processing of each specimen (Afshar et al., 1978). The tissue is also at risk for distortion because of fixing, sectioning, mounting, staining, and dehydration, each of which can compromise tissue structure and/or topological integrity (Calabrese, 2016). The digital nature of MRI enables much more interactive capability and allows for powerful technological manipulations of intrinsic signals, although MRI has traditionally been limited by its relatively low spatial resolution compared to optical microscopy. Thus, conventional MRI, such as that typically used in clinical or research applications with human subjects, is insufficient for rendering detailed models of fine neuroanatomical structure, which is defined by the composition of microscopic cellular and extracellular compartments at scales of organization that are orders of magnitude below the resolution of such conventional MRI acquisitions.

Bridging this gap between the resolution of histology-based methods and the flexibility and resource efficiency of MRI techniques, structural approaches to high-resolution MRI of postmortem specimens allow for efficient acquisition of MR images with unprecedented resolution and image quality. This imaging strategy has been dubbed “magnetic resonance histology” (MRH) (Johnson et al., 2002), appropriating the usual meaning of the term histology to refer to the visualization and analysis of the microscopic anatomy of biological structures – here, by means of high-resolution MRI. Namely, the use of long scan-times, exogenous contrast agents, and specialized imaging hardware have made it possible to acquire datasets and generate images that resolve structural detail that could not be interrogated in conventional *in vivo* human scans.

Regarding *ex vivo* imaging of the human brain and brainstem, previous work has been restricted to specific nuclei or anatomical subregions of the specimens (Aggarwal et al., 2013; Edlow et al., 2012; Henssen et al., 2019), had limited angular resolution (Aggarwal et al., 2013), or looked exclusively at white matter (McNab et al., 2009). Nonetheless, these previous *ex vivo* studies certainly rendered images more detailed than those of conventional *in vivo* MRI, and we aim to build on these prior achievements.

Herein, we present the use of MRH and diffusion tractography (DT) to render a segmented and labeled, high-resolution, 3D digital atlas of the human brainstem, including specific white matter pathways. This publicly available atlas has inherent value as a tool for interactively studying the complex neuroanatomy intrinsic to the human brainstem. Future iterations of this same technique and further development of the user interface should enable applications in neuroanatomical research and neurosurgical planning, particularly as “safe zones” are increasingly recognized and utilized for the neurosurgical treatment of previously intractable lesions (Cavalcanti et al., 2016).

2. Materials and methods

Here, we report the methods used to generate an atlas of the human brainstem using the same MR dataset presented previously by our group (Calabrese et al., 2015c). Thus, the acquisition and dissection of the specimen, the postmortem MRI, and the diffusion data processing have been described in detail previously. Here, we briefly account for the aspects of this approach that are relevant for the diffusion tractography, the segmentation of anatomical regions, and the construction of the atlas. The acquisition of the specimen was approved by the Duke University Health System Institutional Review Board.

2.1. Human brainstem specimen

Approximately 24 h after death, the brain was removed from the calvarium using standard dissection techniques, with section of the central nervous system at the cervical-medullary junction. The brainstem and adjacent deep forebrain structures were isolated from the rest of the forebrain and the cerebellum. The specimen included the entire brainstem through the middle of the pyramidal decussation at the transition between the caudal medulla and the first segment of the cervical spinal cord. The specimen also included most of the diencephalon, internal capsule and medial portions of basal ganglia and basal forebrain nuclei through a coronal plane at the level of the optic chiasm (excluding the preoptic

region of the hypothalamus, the anterior nuclei of the dorsal thalamus, most of the anterior limb of the internal capsule, most of the head of the caudate nucleus, the ventral striatum, and most of the putamen). Distal portions of the cerebellar peduncles were included with the section through their confluence just dorsal-lateral to the basilar pons and pontine tegmentum. Following this dissection, the specimen was immersion-fixed, doped with 1% (5 mM) gadoteridol (ProHance, Bracco Diagnostics, Monroe, Township, NJ), and transferred to a custom-made MRI-compatible tube and immersed in pure liquid fluorocarbon (unbuffered; Galden PFPE, Solvay Plastics, Brussels, Belgium) for imaging to prevent tissue dehydration during the long scans; since liquid fluorocarbon is immiscible, it does not permeate the tissue and has no impact on image contrast.

2.2. Postmortem MRI

MR images were acquired on a 7-Tesla (7T) small animal MRI system controlled with an Agilent console running VNMRJ (Agilent Technologies, Santa Clara, CA). Crucial to the study was a Resonance Research gradient coil providing gradients of 650 mT/m. [For comparison, the human connectome scanners have gradients providing up to 300 mT/m (McNab et al., 2013)]. A 65 mm bespoke quadrature RF coil (transmission and reception) (M2M Imaging, Cleveland, OH) was used to maximize sensitivity.

A 3D gradient echo sequence (TR/TE of 50/10 ms, flip angle (α) of 60°) was used to acquire a 3D anatomic image with 50 μm isotropic spatial resolution. As a consequence, the image matrix was large (1600 × 1100 × 900). The total acquisition time for the gradient echo image was 14 h.

Diffusion data were acquired using a Stesjkal Tanner RF refocused spin echo sequence (TR/TE of 100/33.6 ms). Diffusion weighting was done with half-sine wave forms that exploit the fast rise time of the gradients yielding a width (δ) of 4.7 ms, separation (Δ) of 26 ms, and gradient amplitude (G) of 50.1 G/cm. Single-shell high-angular resolution diffusion imaging (HARDI) data were acquired with 120 unique diffusion directions at $b = 4000$ s/mm^2 and 11 baseline (b0) images dispersed regularly throughout the acquisition. The total acquisition time was 208 h. Upon completion of the scan the individual diffusion-weighted volumes were registered to the baseline images using a pipeline based on the advanced normalization tool kit (ANTs; (http://www.picsl.upenn.edu/ANTS/). The resulting 4D array was 450 × 275 × 275 × 131 with isotropic spatial resolution of 200 μm.

2.3. Diffusion data processing

After initial image reconstruction, all image volumes (anatomic and diffusion) were registered to the first b0 image volume using the affine transformation implemented in ANTs to correct for the linear component of eddy current distortions. The diffusion gradient matrix was corrected using the rotational component of the affine matrices derived from registration of diffusion-weighted images. The registered diffusion data and the corrected gradient matrix were used for all diffusion reconstructions.

The diffusion tensor was calculated at each voxel using a weighted least-squares approach. The diffusion tensor was used to generate various tensor derived scalar images including fractional anisotropy and directionally color-coded (pseudocolored) fractional anisotropy.

An isotropic diffusion-weighted image was generated by taking the average of all diffusion-weighted image volumes.

2.4. Structure segmentation

Segmentation of distinct gray matter and white matter structures in the brainstem and adjacent diencephalon was performed manually by SMA and LTC, with reference to both histological stain-based human brainstem atlases (Büttner-Ennever and Horn, 2014; Paxinos and Huang, 1995) and an optical photography-based human brainstem atlas authored by one of us (LEW) (Williams and White, 2013). The imaging software used for segmentation was Avizo Lite 9.0.1 (http://www.fei.com/software/avizo3d/). Anatomical regions for segmentation were prioritized based on their known functional significance within sensory or motor systems and with respect to their clinical relevance.

A variety of tools within the segmentation software package were used in the actual voxel selection process, including the brush and magic wand tools. To minimize slice-to-slice inconsistency with these selections, the “wrap” function was frequently used to highlight regions lying between manually selected areas. The use of this interpolation tool (which produces more biologically plausible curved interpolations compared to standard linear interpolations) did lead to slight inaccuracies, which then required manual editing with the guidance of an expert neuroanatomist (LEW).

Multiple contrasts (datasets yielding distinct image types) were used in conjunction with one another to provide the most complete segmentation possible for each structure of interest. The contrasts generated from our acquisitions were: isotropic diffusion weighted images (DWI), axial diffusivity (AD) images, radial diffusivity (RD) images, fractional anisotropy images (FA), color FA (FAC) images, gradient recalled echo (GRE) images, and b0 images. The three primary image types that were most useful in the segmentation of gray matter structures (brainstem and diencephalic nuclei) were GRE and DWI, while FA and FAC were most useful in the segmentation of white matter structures (tracts, peduncles, and cranial nerve roots). In addition, to maximize accuracy of segmentation, all three traditional planes of section (axial, coronal, and sagittal), as well as custom planes transverse or parallel to the longitudinal axis of the brainstem, were projected side by side. Selections made on one image type or orientation were translated to all other image types and orientations. Table 1 presents the complete list of gray and white matter structures that were segmented and labeled in the atlas.

2.5. Diffusion tractography

Deterministic DT was performed using DSI Studio (http://dsi-studio.labsolver.org). Image reconstruction was performed using generalized q-sampling imaging (GQI), a method that can be applied to any sampling scheme, including HARDI as used here. A maximum of five fiber orientations were allowed per voxel (Yeh et al., 2011); if the data on a voxel-by-voxel basis did not support fitting with five possible orientations, then a smaller number was used. Thus, having robust data that enabled using the maximum number of fiber orientations is a key advantage. The calculated orientation distribution function was 8-fold tessellated (Baete et al., 2019).

The software calculated an optimal quantitative anisotropy threshold for tract generation (0.02282; based on Otsu's threshold), which we used and kept constant for all fiber pathways. Additionally, the following parameters were kept constant while performing all tracking: termination index qa (quantitative anisotropy), angular threshold 60 (as used previously, e.g. in Edlow et al., 2012), step size 0.10 mm, smoothing 0.00, minimum length 5.0 mm, maximum length 300.0 mm, seed orientation primary, seed position subvoxel, and direction interpolation trilinear. These parameters were chosen based on prior work (e.g., Maier-Hein et al., 2015) and our assessments of tracts with known angular deviations, such as the decussations (midline crossings) of the dentatothalamic projection and the corticospinal tract. The Euler tracking algorithm was used most frequently; for the longest tracts (corticospinal tracts and medial lemnisci), the rk4 algorithm was sometimes utilized because of its integration of fiber direction over three voxels instead of one (Basser et al., 2000).

Tractography was based upon the image segmentation performed in Avizo. Different tracts required different strategies to achieve optimal visualization, depending on which structures had been segmented that could serve as appropriate seed regions or regions of interest (ROIs). Optimization of the representative images was performed through trial and error using differing seed regions, ROIs, regions of avoidance (ROAs – regions of exclusion that allow for elimination of spurious streamlines), and number of target tracts. In most cases, the segmented regions served as the best guides for the tractography, although occasionally new ROIs were drawn in DSI Studio to serve as additional waypoints guiding the tracts in anatomically correct directions. After achieving optimal tract generation, manual refinement in accordance with expert knowledge was often necessary to trim away erroneous tracts (false positives) and present the most accurate fiber bundles. Table 2 lists the tracts that were reconstructed by DT, the parameters used to generate them, and brief descriptions of their clinical relevancies.

For visualization of pathways in the context of the full, three-dimensional brainstem, surface rendering was performed using the FA image with a threshold of 0.01. The 3D rendering of the full segmentation was also completed in DSI Studio, as the program's smoothing functions provided a more realistic view of the brainstem compared to the more voxelized volume rendering of Avizo.

Users may request a 4D nifti stack and the associated gradient tables (b_table) that were used in DSI Studio to construct our tractography. Since the size of the 4D nifti stack package is quite large [4D size (uncompressed) is 6.28GiB = 275 × 225y 450z 121 vol at 16-bit], we suggest the use of Globus for transfer for interested users who would request our datasets for independent processing and analysis.

3. Results

3.1. Brainstem specimen and image resolution

A specimen including the full brainstem and adjacent portions of the deep medial forebrain posterior to the optic chiasm was successfully isolated postmortem. In its full length, the specimen measured approximately 10 cm from its caudal limit at the pyramidal decussation

to its superior limit near the genu of the internal capsule. It measured 5 × 4 cm at its widest plane at the level of the deep forebrain just dorsal to the optic tracts. Fig. 1 shows dorsal and ventral photographs of this specimen after dissection, vascular flushing and fixation, with surface features in both views annotated (Fig. 1).

After utilizing the postmortem MR imaging protocol described in Section 2.2, the resulting anatomic images (GRE) had an isotropic voxel size of 50 μm, which is 8000 times the resolution obtained in a typical clinical acquisition (~1 mm isotropic voxels). The diffusion images (DWI, FA, color FA, AD, and RD) had an isotropic resolution of 200 μm. This resolution for the diffusion images is 1000 times greater than the typical isotropic clinical diffusion resolution of 2 mm isotropic (although a typical anisotropic clinical scan may be 1 × 1 × 3 mm^3 , or 375 times lower resolution than our dataset). This allows for visualization of anatomic detail that is poorly resolved or invisible in clinical MRI of the brainstem. For example, clearly discernible in our GRE dataset are individual fasciculi of the descending corticospinal tracts intercalated amidst the pontine nuclei and the transverse pontocerebellar fibers in the basilar pons (Fig. 2).

3.2. Image segmentation

Ninety different structures in the brainstem were individually delineated, counting left and right forms of the same structures separately (48 structures when left and right structures are consolidated; see Table 1). Three-dimensional volume renderings of the segmentation are shown in Figs. 3A and 3B. For ease of use in the online atlas that we constructed, structure names are organized by anatomical hierarchy according to the ontology adopted by the Allen Brain Atlas (Hawrylycz et al., 2012), with some minor modifications to facilitate navigation and recognition of common neuroanatomical terms.

Different image contrasts highlighting different aspects of the neuroanatomy were used together to most effectively and accurately segment brainstem structures. For example, the GRE allows visualization of finer levels of detail that are much less distinct in the diffusion images, such as the transverse fibers of the pons (Fig. 2), abducens nuclei, and mammillothalamic tracts. The DWI is particularly useful in distinguishing other, larger structures such as the substantia nigra and red nuclei (Fig. 4). These subcortical nuclei have a particularly noticeable hypointensity in DWI due to age- and brain region-dependent depositions of non-heme iron, which enhance the differentiation between gray and white matter at the boundaries of these nuclei (Martin, 2009). Complimenting both of these distinctive datasets, FA images (grayscale and pseudocolored) highlight different white matter tracts, such as the middle cerebellar peduncles, the roots of the trigeminal nerves, and the corticospinal tracts (Fig. 5). Fig. 6 shows images across datasets at the level of the rostral midbrain. This comparison of MRH contrasts (images) highlights the utility of each in differentiating gray matter and white matter structures in the postmortem human brainstem.

The brainstem may be visualized from the three traditional planes of view (axial, coronal, and sagittal) or user-specified deviations from these standard anatomical planes, with selections made in one view becoming visible in the other orthogonal planes. For example, Figs. 2, 4, 5 and 6 show images obtained in a transverse plane that is orthogonal to

the longitudinal axis of the brainstem; this plane is comparable to the presentation of histological sections in most conventional atlases of the human brainstem, but oblique by ~30° (rotated in the anti-clockwise direction) relative to standard *in vivo* MR imaging (e.g., the axial plane defined by the bisection of the anterior and posterior commissures). Additional custom planes were utilized, as shown in Fig. 7. Fig. 7A demonstrates an oblique plane acquired by rotating the "slice" (image) approximately 60° clockwise from the axial plane in order to view the human brainstem in a plane that is parallel to its longitudinal axis. For comparison, Fig. 7B demonstrates a parasagittal plane obtained from the rotated dataset. For segmentation purposes, the transverse plane through the human brainstem was predominantly utilized, but selections were optimized using these different viewing angles and image contrasts.

3.3. Diffusion tractography

As described, the segmented regions were used to guide DT. Ultimately, 11 major white matter pathways were generated and refined (counting both sides of bilateral pathways as one pathway; see Table 2). Among the most robust of the fiber bundles were the corticospinal tracts (Fig. 8) and superior cerebellar peduncles, whereas the medial lemnisci were more challenging to render accurately—especially in the mesencephalic trajectory.

The methods used were robust enough to generate fiber tracts for the roots of the two trigeminal nerves (cranial nerve V) and the two facial nerves (cranial nerve VII), but not sufficient to render adequately the roots of the abducens nerves (cranial nerve VI). Presumably, this was due to the dispersion of rootlets as they course from the abducens nuclei through the base of the pons just lateral to the corticospinal fibers. For similar reasons, we were unable to accurately render the roots of cranial nerves III, IV, VIII, IX, X and XII (cranial nerve XI was not attached to this brainstem specimen given its origins in the upper cervical segments of the spinal cord). Nevertheless, the intramedullary roots of cranial nerves III, IV, VIII, IX, X and XII are discernible, particularly in the GRE contrast, when scrolling through the brainstem volume in the region of these nerve roots.

One of the primary strengths of this dataset lies in its high angular resolution allowing for the visualization of crossing fibers within a voxel. This crossing is demonstrated in the robust decussation of the dentatorubrothalamic tracts (superior cerebellar peduncles) (Fig. 9; see also the decussation of the medullary pyramids in Fig. 8). For some tracts (anterior commissure, posterior commissure, anterior columns of fornix, and roots of the facial nerves), the segmented region was too small to serve as an efficient seed region or ROI alone. In these cases, manual ROIs (typically spheres) were drawn on either end of the structures to effectively "bookend" them and generate tracts more efficiently.

Some of the tracts are not entirely distinct from the white matter structures that contain them. For example, the dentatorubrothalamic tract is part of the superior cerebellar peduncle, and the corticospinal tracts make up only a very small fraction (<5%) of the number of fibers in the cerebral peduncles and internal capsule (Wada et al., 2001). Thus, some of these names and distinctions are less precise than ground-truth fascicular neuroanatomy; but where they are still useful, they have been retained for illustrative purposes.

3.4. Interactive viewer

An interactive viewer was created to enable easy exploration of the multidimensional data set. The viewer is derived from 3D Slicer (Slicer.org), an open source platform that has been designed to support multimodality imaging across all three major desktop platforms (Linux, MacOSX, and Windows). Fig. 10 displays the viewing window at the level of the red nucleus. The application is protocol driven; i.e., there are specific display protocols embedded in the application to facilitate useful modes of interaction. The default protocol allows one to choose two of the available contrasts (GRE, AD, RD, etc.) to display simultaneously in the lower image panes. A guide ("navigational") image in the upper left pane provides an overview of the brainstem in parasagittal planes and interactive sliders defining location and angle of the cross sections in the two contrasts chosen. Clickable buttons under the guide image pane engage the anatomic labels, which will be displayed on all image panes over the different contrasts. Alternatively, clicking on a structure in any one of the image panes will present the outline of the structure's border in each pane and indicate the name of the structure. One of the custom configurations delivered with the atlas for 3D Slicer allows users to load external images or datasets from other sources in the fourth window (upper right in Fig. 10). As an example, we have included a copy of the standard ICBM 152 human brain dataset (version: 2009b Nonlinear Symmetric) from the Montreal Neurological Institute (MNI) (Fonov et al., 2011, 2009), which is shown for comparison at approximately the same neuroanatomical level as our datasets in the lower panes.

Other protocols ("layouts") in 3D Slicer allows users to load volume-renderings of the structures segmented in the atlas and/or reconstructed tracts (see Table 2) along with sectional images of different MR contrasts. For example, Fig. 11 features the reconstruction of the corticospinal tracts bilaterally with transverse sections at two different levels (caudal diencephalon in DWI and caudal pons in color FA) illustrating the passage of corticospinal tract fibers through the posterior limb of internal capsule into the cerebral peduncle (DWI image) and the more caudal intercalation of fibers among pontine nuclei and pontocerebellar fibers (color FA image). Users may interact with these images and tracts and vary the rotational perspective, translation and magnification of the brainstem.

3.5. Accessing the Atlas

A bundle comprising the atlas viewer application, brainstem data (scalar images, images for each contrast, the generated tracts, and the segmented label set), and user instructions is accessible from the website associated with the Duke Center for In Vivo Microscopy (https://civmvoxport.vm.duke.edu/voxbase/login.php?return_url=%2Fvoxbase%2F)[1]. At present, the atlas is available for set-up on Windows-based machines and Apple computers (configurations for other platforms remain in development) following installation of 3D Slicer. For full functionality of the interactive 3D atlas, the system requirements are: (1) Windows or macOS operating systems; (2) an integrated graphics card is sufficient for basic visualization; but a discrete graphics card

[1]Users may install the atlas, access these data, and interact with the curated datasets by navigating to the website and requesting access credentials.

(NVidia GPU) with OpenGL 3 support is recommended for interactive 3D volume rendering and fast rendering of curated DT tracts; and (3) GPU texture memory (VRAM) should be larger than the largest dataset (GRE = 3.56 GB), ideally by a factor of two. Artifacts may appear in rendering of images with lower performance GPUs. Detailed set-up instructions and user guidance is provided in Supplemental Materials.

4. Discussion

Here we presented an ultra-high resolution atlas of the intact human brainstem using *ex-vivo* MRH to circumvent the limitations of traditional histological techniques and *in vivo*-grade MRI. After image acquisition, we then used these high-resolution data for segmentation of numerous gray matter and white matter structures and as the basis for fiber tractography of several major white matter pathways, including multiple tracts with neurosurgical significance. Compared to the several most recent diffusion tensor imaging (DTI) studies of the human brainstem (Aggarwal et al., 2013; Axer et al., 2011; Bianciardi et al., 2016; Edlow et al., 2012; Ford et al., 2013; Kamali et al., 2009; McNab et al., 2009; Meola et al., 2016; Prats-Galino et al., 2012; Sclocco et al., 2018; Tang et al., 2018; Lechanoine, 2021), the atlas presented here features the highest high resolution data—both spatial and angular—along the full length of the brainstem.

4.1. Improvements upon previous efforts in human brainstem imaging

There have been efforts to create high-resolution 3D maps of the human brainstem for several years now. Refining a non-MRI technique born in the late 1990s, prior to advanced MRI techniques becoming more widespread, one team took serial sections of six human brainstems and used polarized light to estimate the three-dimensional path of fiber tracts, followed by mathematical alignment/reconstruction and finally digitization of the images, ultimately achieving a resolution of 64 × 64 × 100 μm (Axer et al., 2011). Although this process is capable of providing detailed images, it is labor-intensive, restricted to a single contrast, and subject to more tiers of computational reconstruction than MR. MRH as described here also rendered anatomic images at the higher isotropic resolution of 50 μm.

Ex vivo MRI has previously been used to analyze postmortem human brainstems, albeit with limitations relative to the work presented herein. Very recently, one team scanned an *ex vivo* human brainstem specimen at 11.7T, rendering diffusion and anatomic isotropic resolutions of 300 and 100 μm, respectively (Lechanoine, 2021). They also provide a rigorously-documented segmentation of 99 structures in their easy-access online platform. Our work complements this by adding higher resolution, more image contrasts, and fiber tractography. Earlier studies focused only on subregions or selected levels of the brainstem. Edlow et al. (2012) utilized postmortem HARDI and acquired 60 different directional gradients (half our parameter in their Cases 1 and 2; although their Case 3 was an *in vivo* scan with 120 directional gradients), but only analyzed those regions and tracts involved in the ascending reticular activating system, achieved a best resolution of 562 × 609 × 641 μm^3 (approximately 1750x lower resolution than our GRE images). Moving beyond the brainstem, another group used 3D diffusion-weighted steady-state free precession (DW-SSP)

to image white matter of the entire postmortem human brain; this technique on their 3T scanner ultimately yielded an isotropic resolution of 800 μm (McNab et al., 2009).

As a key precursor to our work, using postmortem MR, Aggarwal et al. (2013) performed DTI of the entire brainstem at high spatial resolution (255 μm isotropic voxels), but their specimen did not include the thalamus or adjacent deep forebrain (Aggarwal et al., 2013)—important strengths of our work here, as they contain continuations of several key white matter pathways and have clinical relevance as localizations for deep brain stimulation (DBS) targets (Calabrese, 2016). After this full brainstem scan, both the medulla and cervicomedullary junction were dissected away and imaged separately to achieve the excellent spatial resolutions of 170 μm and 125 μm isotropic voxels, respectively (with the natural cost of loss of continuity from the rest of the brainstem). The most significant difference between this study and ours was the lower *angular* resolution; their diffusion images of the entire brainstem were taken from 30 diffusion directions (less for the two dissected subregions) compared to our 120 directions. Because Aggarwal et al. (2013) performed DTI with a single tensor per voxel and thus could not undertake crossing fiber tractography, our strategy renders a more accurate atlas that, in future iterations, may be used for more detailed and accurate neurosurgical planning (as discussed in Section 4.2). Previous work on the high resolution atlas of the mouse brain demonstrated that over 72% of voxels were found to have two or more fiber populations with distinct orientations; in light of this fact, it is crucial to recognize the importance of accounting for multiple fiber populations even with high spatial resolution (Calabrese et al., 2015b). Nonetheless, the tractography presented here is associated with its own set of drawbacks (see Section 4.4).

Complementing these small-sample. *ex vivo* studies, recent efforts have shown improvement with *in vivo* imaging techniques for fiber tractography. Using 7T functional MRI, Bianciardi et al. (2016) achieved a 1.1 mm isotropic resolution of the brain and analyzed functional connectivity of brainstem nuclei to the rest of the brain. Setsompop et al. (2018) achieved 0.66–0.76 mm isotropic resolution of the whole brain on a 3T scanner using generalized slice-dithered enhanced resolution. Meola et al. (2016) applied advanced diffusion MRI fiber tracking techniques to a brainstem atlas based on *in vivo* scans of 488 patients from the Human Connectome Project (HCP). Subsequently, and addressing a weakness of this first study, Tang et al. (2018) implemented extensive quality control protocols to exclude HCP subjects with severe brainstem distortions. This facilitated a more focused study of 20 HCP cases with minimal distortion that allowed for successful reconstruction of 23 fiber bundles from which probabilistic atlases in the MNI152 space were generated (Tang et al., 2018). Advanced fiber tracking methods led to diffusion data being collected from 270 sampling directions, but these images came from clinical 3T scans, with a T1-weighted isotropic spatial resolution of 0.7 mm [in the Tang et al. (2018) study] and a diffusion MRI isotropic spatial resolution of 1.25 mm (both aforementioned studies). These works provide some of the first high-quality, population-based *in vivo* tractography of the human brainstem, thus providing an important complement to *ex vivo* work presented here and previously. We build on these results by offering higher spatial resolution and providing a more complete segmentation of gray matter structures with the goal of creating a more comprehensive atlas.

The present atlas goes beyond previous attempts to visualize the whole brainstem, not only via state-of-the-science spatial and angular resolution, but also through interactive and three-dimensional volume rendering. Users will be able to juxtapose numerous different image contrasts to highlight various anatomical features, scroll through hundreds of slices with ease, manipulate the images on the screen (rotation, zoom, translation), and add and remove structures and pathways for clarity. An additional, critical advantage of this work lies in its high angular resolution, enabling users to change the angle of the plane of visualization to better match those of other images for comparison, or to enable unique planes of view. Together, these capabilities render an experience that is in stark contrast to how one typically uses microscope slides or a 2D histology atlas, slowly flipping through pages and trying to keep an eye on specific structures as they change shape and location in discontinuous fashion. Even if digitized, histological atlases have inherent limitations that typically prevent such facile and multidimensional visualization of neural structures (Williams and White, 2013). These features of our atlas have obvious applications today in educational settings, and future iterations of this workflow may serve as the basis for the creation of a clinically-useful atlas for neurosurgical planning.

4.2. Clinical relevance

The brainstem is located at a critical anatomic juncture, connecting the cerebrum to the spinal cord and cerebellum, with lesions in this region leading to a wide spectrum of neurological disorders (Donaldson et al., 2006). In vivo imaging of the brainstem is limited because of the region's small size and complexity—MRI of the brainstem is thus particularly susceptible to low-resolution images, partial volume effects, and eddy-current distortions (Le Bihan et al., 2006). Detailed mapping of brainstem structures will, then, be of significant clinical importance. Because it is also one of the most conserved regions of the human brain and its structure is relatively consistent across people (Afshar et al., 1978), creating pilot atlases based on one person does not carry as much of the typical risk accompanying models derived from small samples.

The ability to accurately visualize the spatial relationships between nuclei and the nearby white matter tracts (as in Fig. 8) will be powerful in the neurosurgical operating room, allowing for unprecedented detail in surgical planning: clinicians may visualize nuclei as potential surgical targets, probe in three-dimensional space what structures neighbor these potential targets and should be avoided, predict what side effects may occur due to electrode proximity to various fiber tracts, and more. Especially in functional neurosurgery, in which many operations do not involve navigating around significant structural malformation such as that seen in tumor resection, brain atlases derived from typical human neuroanatomy may be especially useful. For example, in the case of DBS, a procedure commonly used to alleviate motor abnormalities associated with Parkinson's disease and essential tremor, accuracy of electrode placement within the deep forebrain or brainstem is critical for therapeutic efficacy (Calabrese et al., 2015c). Moreover, though literature regarding DBS targets specifically in the brainstem is more sparse relative to counterparts in the thalamus and basal ganglia, this is rapidly changing—a recent systematic review (Elias et al., 2020) identified 164 studies on the topic, with the most promising targets including "the pedunculopontine nucleus for relief of axial motor deficits, periaqueductal/periventricular

grey for the management of central neuropathic pain, and ventral tegmental area for treatment of cluster headaches."

In today's operating room, targeting of DBS electrodes is based on selecting anatomic landmarks from clinical scans and overlaying them onto a morphometric, two-dimensional atlas. At many centers, it is considered imperative that awake intraoperative testing and audible monitoring of the neurophysiological recording be performed as the microelectrode is advanced through the brain, in conjunction with brain imaging. Using this dual technique, DBS can be effective—but there is significant room for improvement. Though technologies are constantly evolving, one widely-used stereotaxic reference atlas for surgical planning is based in conventional histology (Schaltenbrand et al., 1977). This atlas benefits from the high in-plane resolution of conventional histology and light microscopy techniques (200–700 nm), but the distortions from fixing, sectioning, and staining tissue (Calabrese, 2016), combined with a loss of 3D spatial awareness, limit its utility. The digital nature of MRI grants images more interactive capabilities and allows for powerful technological manipulations.

In light of these advantages, approaches to surgical planning have transitioned away from conventional histology and towards MRI (Fonov et al., 2011; Mazziotta et al., 2001; Oishi et al., 2010), and the imaging strategy presented here may represent a novel way to approach this challenge. New surgical systems, such as Brainlab (BrainLAB AG; Munich, Germany), have incorporated their own proprietary DTI atlas, allowing the surgeon to incorporate fiber tracts into the surgical plan. Many centers are moving to DBS under general anesthesia that is completely dependent on imaging for targeting, highlighting the importance of integrating high-resolution diffusion imaging into the clinical workflow. Furthermore, directional DBS leads are now available, allowing current steering and use of electrical field models to represent volumes of tissue activation. These advances will make it possible to provide highly accurate targeting and effective neurostimulation of the desired brain targets—with success again dependent on accurate imaging.

The visualization of white matter tracts, as done here, will be critical in enhancing the effectiveness of DBS, as the white matter environment surrounding DBS target nuclei plays a large role in the mechanism of this neuromodulation therapy (Coenen et al., 2012). Already, the power of this high-resolution dataset has been demonstrated by retroactively illustrating a correlation between positive patient outcomes and proximity of DBS electrodes to areas that would have been surgically recommended by this model for essential tremor (Calabrese et al., 2015c). The utility of such a high resolution atlas, including its gray matter components, will continue to grow as do the indications for DBS; for example, initial results also demonstrate promise for the procedure in treating intractable epilepsy (by targeting the anterior nucleus of thalamus, closest to the mammillothalamic tract (Krishna et al., 2016)), Alzheimer's Disease (through the fornix (Jakobs et al., 2019)), obesity (Franco et al., 2016), and a wide variety of psychiatric conditions including major depressive disorder and alcohol/drug addiction (Harmsen et al., 2019). Brainstem visualization is also critical for other neurosurgical interventions (other than DBS), such as nucleus caudalis dorsal root entry zone (NC DREZ) lesioning, a treatment for various forms of chronic,

medically refractory facial pain (e.g., trigeminal neuropathic pain, post-herpetic neuralgia, deafferentation pain, etc.) (Kanpolat et al., 2008).

4.3. Creating a community atlas using a packaged application

We hope that by publishing this atlas online, we are taking the first step toward engaging a community of scholars and learners that can collectively render a more complete, precise and accurate neuroanatomical atlas of the postmortem human brainstem. As presented here, the atlas can be used for those who want to explore the brainstem without a complex computer infrastructure. In the future, it may be possible to build a component library that can be downloaded to enable a deeper probe into the data, thus illuminating opportunities for further development (e.g., additional segmentations; improved ontologies; new DT and curation of additional tracts). End users would be able to create novel libraries that would be served in our atlas platform and shared broadly within the community of users. Already, these data have been used to thoroughly map the subcortical auditory system (Epprecht et al., 2020; Sitek et al., 2019). Through mutual appreciation of and discussion about different neuroanatomical delineations, we hope this project represents the first step toward creating a dynamic “community atlas” used by scientists, learners, and clinicians alike. Along with the new atlas presented by Lechanoine et al. (Lechanoine et al., 2021), our atlas should serve well the community of investigators and clinicians interrogating the complex 3D neuroanatomy of the human brainstem.

4.4. Limitations and future directions

This work has a number of limitations; foremost among them is the fact that these datasets derive from one patient. This remains an important limitation of our present work, despite the relative anatomical consistency of the brainstem among specimens compared to the well-known morphological variation of the human cerebrum. Nevertheless, the consistency of the human brainstem among subjects warrants further empirical study. For example, we did observe lateralized differences in the thickness of fiber bundles for the dentatorubrothalamic tracts, medial lemnisci, trigeminal pathways, and mammillothalamic tracts in our DT datasets. Future efforts should aim to curate a collection of individual brainstems scanned using the MRH protocols; such a sample is necessary to address questions of reproducibility and consistency with quantitative morphometry applied to the level of discrete nuclei, white matter structures and neuroanatomical tracts. A complimentary goal is creation of an average atlas based on such datasets from multiple individuals.

The *ex vivo* nature of the specimen also introduces some risk of anatomical inaccuracy. Formalin fixation and even brain extraction are both known to affect total brain volume; however, one study examining a 70-day 10% formalin fixation of human brain specimens showed only a 3.3% ± 0.5% volume reduction (Schulz et al., 2011). This 70-day fixation is much lengthier than the two-week fixation used here, so we can expect that our differences would be even smaller (Calabrese et al., 2015a). Moreover, to counter the concern of the approximately fourfold loss of water diffusivity in *ex vivo* brain tissues (Alexander et al., 2010; Dyrby et al., 2011), we used a b-value that is four times higher, thus resulting in diffusivity similar to that of *in vivo* specimens. We additionally minimized the potential for postmortem changes by removing the brain within 24 h of the patient’s death. To better

understand how postmortem DT of the cerebrum quantitatively compares to dissection results, one previous group developed a technique called FIBRASCAN (Zemmoura et al., 2014). Here, researchers performed Klingler's dissection of brain hemispheres while taking serial laser scans of the tissue surface and ultimately reconstructing the fiber tracts and registering them onto *ex vivo* MRI space. Future iterations of similar work, with an emphasis on the brainstem, may help confirm the validity of our MRH atlas.

With such high resolution data, the segmentation itself—in deciding where one structure begins and another ends—is inherently subjective and often beyond the resolution limits of the present data. One important next step in the development of our atlas will be the sectioning and histological processing of the very specimen that was the subject of our MR imaging. Such an endeavor is beyond the scope of our present study. When it is possible to commit this specimen to such terminal analysis, it will be possible to align the MR datasets with optical scans of histological sections stained to reveal neuroanatomical structure. Then, it will be possible to make direct comparisons between localized physicochemical properties of the human brainstem as revealed by means of MR imaging and the microscopic anatomy revealed by conventional histological and histochemical means. We hope that conversation sparked by the "community atlas" will help to align our present segmentation with expert consensus in future updates and iterations, even as we work toward further development of multi-dimensional aligment of MR imaging and more conventional histologic analyses of the same human brainstem.

DT also comes with inherent limitations. Through an international tractography challenge across 20 different research groups, Maier-Hein et al. (2017) encouragingly demonstrated that most tractograms do include some ground truths; however, there were routinely more invalid bundles than valid bundles. These teams used orientation information alone to generate bundles; here, we increased accuracy of fiber tracts by using strategically-chosen seed ROIs/ROAs and expert knowledge of ground truths to refine our tractography, although this does decrease direct reproducibility of the tracts. Importantly, performing this extra step still does not allow us to definitively claim the rendered tracts as ground truths—they are simply our best efforts given the limitations inherent in the present state of the science of DT. As improved DT methodologies arise in the future, we are optimistic that they could be utilized with high-resolution data similar to that used herein to ameliorate the issue of false-positive tracts. We also here used deterministic tractography, in which paths are simply generated using the most likely fiber directions (derived from the eigenvector of the largest eigenvalue) (Coenen et al., 2012). Future efforts should incorporate confidences in the estimated tracts via probabilistic tractography. Finally, we acknowledge that specific scanning techniques, tractography parameters, and other variables affect how certain white matter pathways are reconstructed; for example, we did not render all cranial nerves, but previous work with deterministic tractography has demonstrated that it is possible to visualize all 12 cranial nerves in certain circumstances (Yoshino et al., 2016). Indeed, the intramedullary roots of cranial nerves III-X and XII are visible in the GRE contrast (the roots of cranial nerve XI are mainly in the rostral cervical segments of the spinal cord, which is caudal to the inferior limit of our specimen).

DT is also limited by the fact that different imaging protocols can yield different results. This has driven efforts to better understand tradeoffs in imaging parameters, such as how much acquisition time should be spent on increasing spatial resolution versus q-space sampling (Calabrese et al., 2014). Furthermore, DT does not always correspond with findings derived from conventional neuronal tract-tracing experiments that yield results with axonal or neuronal resolution. DT is bidirectional rather than unidirectional, and the signals —even at the spatial and angular resolution that we obtained—correspond to bundles or fascicles of axons, rather than individual axons (Calabrese et al., 2015b). Because of these limitations, biological interpretation of DT data remains a notable challenge in the MRI community. Nevertheless, MRH and DT provide complementary means for interrogating structure in the human brain through digitally and non-destructively mapping the intrinsic signals derived from such multimodal MR acquisitions. With further technological advances, it is our hope that such methods may more fully characterize the connectome of the human brainstem, which is undoubtedly one of the most complex and clinically significant of all divisions of the human central nervous system.

5. Conclusion

We used postmortem imaging to present the highest-ever resolution MRI atlas of the full human brainstem, including segmentation of 90 structures and tractography of 11 white matter pathways. This atlas is available online for interactive 3D use with the aim of creating a dynamic community atlas. There are natural applications today in education and anatomical study, and similar techniques may be used in the future to render an atlas useful for neuroanatomical research and neurosurgical planning across a wide variety of procedures. Future efforts should build on this work by using multiple patients and probabilistic diffusion tractography techniques. These and other deeper efforts are needed to create an optimized, final product that may serve as the foundation for future neuroanatomical studies of the intact human brainstem as well as clinical studies assessing feasibility and efficacy of such an atlas’s implementation in the neurosurgical operating room.

Supplementary Material

Refer to Web version on PubMed Central for supplementary material.

Acknowledgments

We thank Lucy Upchurch for her essential role in developing and maintaining the computer architecture and Steve Noh for his assistance in segmentation.

Funding sources

This work was supported by the National Institutes of Health [1R01NS096720-01A1 1S10OD010683-015, P41-EB015897–28].

References

Afshar F, Watkins ES, Yap JC, 1978. Stereotaxic Atlas of the Human Brainstem and Cerebellar Nuclei. A Variability Study. Raven Press, New York.

Aggarwal M, Zhang J, Pletnikova O, Crain B, Troncoso J, Mori S, 2013. Feasibility of creating a high-resolution 3D diffusion tensor imaging based atlas of the human brainstem: a case study at 11.7 T. Neuroimage74, 117–127. [PubMed: 23384518]

Alexander DC, Hubbard PL, Hall MG, Moore EA, Ptito M, Parker GJ, Dyrby TB, 2010. Orientationally invariant indices of axon diameter and density from diffusion MRI. Neuroimage52, 1374–1389. [PubMed: 20580932]

Axer H, Beck S, Axer M, Schuchardt F, Heepe J, Flucken A, Axer M, Prescher A, Witte OW, 2011. Microstructural analysis of human white matter architecture using polarized light imaging: views from neuroanatomy. Front. Neuroinform5, 28. [PubMed: 22110430]

Baete SH, Cloos MA, Lin YC, Placantonakis DG, Shepherd T, Boada FE, 2019. Fingerprinting Orientation Distribution Functions in diffusion MRI detects smaller crossing angles. Neuroimage198, 231–241. [PubMed: 31102735]

Basser PJ, Pajevic S, Pierpaoli C, Duda J, Aldroubi A, 2000. In vivo fiber tractography using DT-MRI data. Magn. Reson. Med44, 625–632. [PubMed: 11025519]

Bianciardi M,Toschi N,Eichner C,Polimeni JR,Setsompop K,Brown EN, Hamalainen MS, Rosen BR, Wald LL, 2016. In vivo functional connectome of human brainstem nuclei of the ascending arousal, autonomic, and motor systems by high spatial resolution 7-Tesla fMRI. MAGMA29, 451–462. [PubMed: 27126248]

Büttner-Ennever JA, Horn AKE, 2014. Olszewski and Baxter's Cytoarchitecture of the Human Brainstem. S. Karger AG, Basel.

Calabrese E, 2016. Diffusion tractography in deep brain stimulation surgery: a review. Front. Neuroanat10, 45. [PubMed: 27199677]

Calabrese E, Badea A, Coe CL, Lubach GR, Shi Y, Styner MA, Johnson GA, 2015a. A diffusion tensor MRI atlas of the postmortem rhesus macaque brain. Neuroimage117, 408–416. [PubMed: 26037056]

Calabrese E, Badea A, Coe CL, Lubach GR, Styner MA, Johnson GA, 2014. Investigating the tradeoffs between spatial resolution and diffusion sampling for brain mapping with diffusion tractography: time well spent?Hum. Brain Mapp35, 5667–5685. [PubMed: 25044786]

Calabrese E, Badea A, Cofer G, Qi Y, Johnson GA, 2015b. A diffusion MRI tractography connectome of the mouse brain and comparison with neuronal tracer data. Cereb. Cortex25, 4628–4637. [PubMed: 26048951]

Calabrese E, Hickey P, Hulette C, Zhang J, Parente B, Lad SP, Johnson GA, 2015c. Postmortem diffusion MRI of the human brainstem and thalamus for deep brain stimulator electrode localization. Hum. Brain Mapp36, 3167–3178. [PubMed: 26043869]

Cavalcanti DD, Preul MC, Kalani MY, Spetzler RF, 2016. Microsurgical anatomy of safe entry zones to the brainstem. J. Neurosurg124, 1359–1376. [PubMed: 26452114]

Chung K, Wallace J, Kim SY, Kalyanasundaram S, Andalman AS, Davidson TJ, Mirzabekov JJ, Zalocusky KA, Mattis J, Denisin AK, Pak S, Bernstein H, Ramakrishnan C, Grosenick L, Gradinaru V, Deisseroth K, 2013. Structural and molecular interrogation of intact biological systems. Nature497, 332–337. [PubMed: 23575631]

Coenen VA, Schlaepfer TE, Allert N, Madler B, 2012. Diffusion tensor imaging and neuromodulation: DTI as key technology for deep brain stimulation. Int. Rev. Neurobiol107, 207–234. [PubMed: 23206684]

Donaldson SS, Laningham F, Fisher PG, 2006. Advances toward an understanding of brainstem gliomas. J. Clinic. Oncol24, 1266–1272.

Dyrby TB, Baare WF, Alexander DC, Jelsing J, Garde E, Sogaard LV, 2011. An ex vivo imaging pipeline for producing high-quality and high-resolution diffusion-weighted imaging datasets. Hum. Brain Mapp32, 544–563. [PubMed: 20945352]

Edlow BL, Takahashi E, Wu O, Benner T, Dai G, Bu L, Grant PE, Greer DM, Greenberg SM, Kinney HC, Folkerth RD, 2012. Neuroanatomic connectivity of the human ascending arousal system critical to consciousness and its disorders. J. Neuropathol. Exp. Neurol71, 531–546. [PubMed: 22592840]

Elias GJB, Loh A, Gwun D, Pancholi A, Boutet A, Neudorfer C, Germann J, Namasivayam A, Gramer R, Paff M, Lozano AM, 2020. Deep brain stimulation of the brainstem. Brain.

Epprecht L, Qureshi A, Kozin ED, Vachicouras N, Huber AM, Kikinis R, Makris N, Brown MC, Reinshagen KL, Lee DJ, 2020. Human cochlear nucleus on 7 tesla diffusion tensor imaging: insights into micro-anatomy and function for auditory brainstem implant surgery. Otol. Neurotol41, e484–e493. [PubMed: 32176138]

Fonov V, Evans AC, Botteron K, Almli CR, McKinstry RC, Collins DLBrain Development Cooperative, G., 2011. Unbiased average age-appropriate atlases for pediatric studies. Neuroimage54, 313–327. [PubMed: 20656036]

Fonov VS, Evans AC, McKinstry RC, Almli CR, Collins DL, 2009. Unbiased nonlinear average age-appropriate brain templates from birth to adulthood. Neuroimage47, S102.

Ford AA, Colon-Perez L, Triplett WT, Gullett JM, Mareci TH, Fitzgerald DB, 2013. Imaging white matter in human brainstem. Front. Hum. Neurosci7, 400. [PubMed: 23898254]

Franco R, Fonoff ET, Alvarenga P, Lopes AC, Miguel EC, Teixeira MJ, Damiani D, Hamani C, 2016. DBS for Obesity. Brain Sci. 6.

Harmsen IE, Elias GJB, Beyn ME, Boutet A, Pancholi A, Germann J, Mansouri A, Lozano CS, Lozano AM, 2019. Clinical trials for deep brain stimulation: current state of affairs. Brain Stimul.

Hawrylycz MJ, Lein ES, Guillozet-Bongaarts AL, Shen EH, Ng L, Miller JA, van de Lagemaat LN, Smith KA, Ebbert A, Riley ZL, Abajian C, Beckmann CF, Bernard A, Bertagnolli D, Boe AF, Cartagena PM, Chakravarty MM, Chapin M, Chong J, Dalley RA, David Daly B, Dang C, Datta S, Dee N, Dolbeare TA, Faber V, Feng D, Fowler DR, Goldy J, Gregor BW, Haradon Z, Haynor DR, Hohmann JG, Horvath S, Howard RE, Jeromin A, Jochim JM, Kinnunen M, Lau C, Lazarz ET, Lee C, Lemon TA, Li L, Li Y, Morris JA, Overly CC, Parker PD, Parry SE, Reding M, Royall JJ, Schulkin J, Sequeira PA, Slaughterbeck CR, Smith SC, Sodt AJ, Sunkin SM, Swanson BE, Vawter MP, Williams D, Wohnoutka P, Zielke HR, Geschwind DH, Hof PR, Smith SM, Koch C, Grant SGN, Jones AR, 2012. An anatomically comprehensive atlas of the adult human brain transcriptome. Nature489, 391–399. [PubMed: 22996553]

Henssen D, Kuppens D, Meijer FJA, van Cappellen van Walsum AM, Temel Y, Kurt E, 2019. Identification of the pedunculopontine nucleus and surrounding white matter tracts on 7T diffusion tensor imaging, combined with histological validation. Surg. Radiol. Anat41, 187–196. [PubMed: 30382329]

Jakobs M, Lee DJ, Lozano AM, 2019. Modifying the progression of Alzheimer's and Parkinson's disease with deep brain stimulation. Neuropharmacology, 107860. [PubMed: 31765650]

Johnson GA, Cofer GP, Gewalt SL, Hedlund LW, 2002. Morphologic phenotyping with MR microscopy: the visible mouse. Radiology222, 789–793. [PubMed: 11867802]

Kamali A, Kramer LA, Butler IJ, Hasan KM, 2009. Diffusion tensor tractography of the somatosensory system in the human brainstem: initial findings using high isotropic spatial resolution at 3.0 T. Eur. Radiol19, 1480–1488. [PubMed: 19189108]

Kanpolat Y, Tuna H, Bozkurt M, Elhan AH, 2008. Spinal and nucleus caudalis dorsal root entry zone operations for chronic pain. Neurosurgery62, 235–242 discussion 242-234. [PubMed: 18424991]

Krishna V, King NK, Sammartino F, Strauss I, Andrade DM, Wennberg RM, Lozano AM, 2016. Anterior nucleus deep brain stimulation for refractory epilepsy: insights into patterns of seizure control and efficacious target. Neurosurgery.

Le Bihan D, Poupon C, Amadon A, Lethimonnier F, 2006. Artifacts and pitfalls in diffusion MRI. J. Magn. Reson. Imaging24, 478–488. [PubMed: 16897692]

Lechanoine Francoise, et al., 2021. WIKIBrainStem: An online atlas to manually segment the human brainstem at the mesoscopic scale from ultrahigh field MRI. NeuroImage236, 118080. doi:10.1016/j.neuroimage.2021.118080, In press. [PubMed: 33882348]

Maier-Hein K, Neher P, Houde J-C, Caruyer E, Daducci A, Dyrby T, Stieltjes B, Descoteaux M, 2015. Tractography Challenge ISMRM 2015 Data. Zenodo.

Maier-Hein KH, Neher PF, Houde JC, Cote MA, Garyfallidis E, Zhong J, Chamberland M, Yeh FC, Lin YC, Ji Q, Reddick WE, Glass JO, Chen DQ, Feng Y, Gao C, Wu Y, Ma J, He R, Li Q, Westin CF, Deslauriers-Gauthier S, Gonzalez JOO, Paquette M, St-Jean S, Girard G, Rheault F, Sidhu J, Tax CMW, Guo F, Mesri HY, David S, Froeling M, Heemskerk AM, Leemans A, Bore A, Pinsard B, Bedetti C, Desrosiers M, Brambati S, Doyon J, Sarica A, Vasta R, Cerasa A, Quattrone A, Yeatman J, Khan AR, Hodges W, Alexander S, Romascano D, Barakovic M, Auria A, Esteban

O, Lemkaddem A, Thiran JP, Cetingul HE, Odry BL, Mailhe B, Nadar MS, Pizzagalli F, Prasad G, Villalon-Reina JE, Galvis J, Thompson PM, Requejo FS, Laguna PL, Lacerda LM, Barrett R, Dell'Acqua F, Catani M, Petit L, Caruyer E, Daducci A, Dyrby TB, Holland-Letz T, Hilgetag CC, Stieltjes B, Descoteaux M, 2017. The challenge of mapping the human connectome based on diffusion tractography. Nat. Commun8, 1349. [PubMed: 29116093]

Martin WR, 2009. Quantitative estimation of regional brain iron with magnetic resonance imaging. Parkinsonism Relat. Disord15 (Suppl 3), S215–S218. [PubMed: 20082994]

Mazziotta J, Toga A, Evans A, Fox P, Lancaster J, Zilles K, Woods R, Paus T, Simpson G, Pike B, Holmes C, Collins L, Thompson P, MacDonald D, Iacoboni M, Schormann T, Amunts K, Palomero-Gallagher N, Geyer S, Parsons L, Narr K, Kabani N, Le Goualher G, Boomsma D, Cannon T, Kawashima R, Mazoyer B, 2001. A probabilistic atlas and reference system for the human brain: international Consortium for Brain Mapping (ICBM). Philos. Trans. R. Soc. Lond. B356, 1293–1322. [PubMed: 11545704]

McNab JA, Edlow BL, Witzel T, Huang SY, Bhat H, Heberlein K, Feiweier T, Liu K, Keil B, Cohen-Adad J, Tisdall MD, Folkerth RD, Kinney HC, Wald LL, 2013. The Human Connectome Project and beyond: initial applications of 300 mT/m gradients. Neuroimage80, 234–245. [PubMed: 23711537]

McNab JA, Jbabdi S, Deoni SC, Douaud G, Behrens TE, Miller KL, 2009. High resolution diffusion-weighted imaging in fixed human brain using diffusion-weighted steady state free precession. Neuroimage46, 775–785. [PubMed: 19344686]

Meola A, Yeh FC, Fellows-Mayle W, Weed J, Fernandez-Miranda JC, 2016. Human Connectome-Based Tractographic Atlas of the Brainstem Connections and Surgical Approaches. Neurosurgery79, 437–455. [PubMed: 26914259]

Oishi K, Faria AV, van Zijl PCM, Mori S, 2010. MRI Atlas of Human White Matter, 2nd ed. Academic Press, San Diego.

Paxinos G, Huang X, 1995. Atlas of the Human Brainstem. Academic Press, San Diego.

Prats-Galino A, Soria G, de Notaris M, Puig J, Pedraza S, 2012. Functional anatomy of subcortical circuits issuing from or integrating at the human brainstem. Clin. Neurophysiol123, 4–12. [PubMed: 22055838]

Schaltenbrand G, Wahren W, Hassler R, 1977. Atlas For Stereotaxy of the Human Brain. Thieme, Stuttgart.

Schulz G, Crooijmans HJ, Germann M, Scheffler K, Muller-Gerbl M, Muller B, 2011. Three-dimensional strain fields in human brain resulting from formalin fixation. J. Neurosci. Methods202, 17–27. [PubMed: 21889536]

Sclocco R, Beissner F, Bianciardi M, Polimeni JR, Napadow V, 2018. Challenges and opportunities for brainstem neuroimaging with ultrahigh field MRI. Neuroimage168, 412–426. [PubMed: 28232189]

Setsompop K, Fan Q, Stockmann J, Bilgic B, Huang S, Cauley SF, Nummenmaa A, Wang F, Rathi Y, Witzel T, Wald LL, 2018. High-resolution in vivo diffusion imaging of the human brain with generalized slice dithered enhanced resolution: simultaneous multislice (gSlider-SMS). Magn. Reson. Med79, 141–151. [PubMed: 28261904]

Sitek KR, Gulban OF, Calabrese E, Johnson GA, Lage-Castellanos A, Moerel M, Ghosh SS, De Martino F, 2019. Mapping the human subcortical auditory system using histology, postmortem MRI and in vivo MRI at 7T. Elife8.

Tang Y, Sun W, Toga AW, Ringman JM, Shi Y, 2018. A probabilistic atlas of human brainstem pathways based on connectome imaging data. Neuroimage169, 227–239. [PubMed: 29253653]

Wada A, Goto J, Goto N, Kawamura N, Matsumoto K, 2001. Are there one million nerve fibres in the human medullary pyramid?Okajimas Folia Anat. Jpn77, 221–224. [PubMed: 11392010]

Williams SM, White LE, 2013. Sylvius 4 Online: An Interactive Atlas and Visual Glossary of Human Neuroanatomy. Sinauer Associates, Inc.

Yeh FC, Wedeen VJ, Tseng WY, 2011. Estimation of fiber orientation and spin density distribution by diffusion deconvolution. Neuroimage55, 1054–1062. [PubMed: 21232611]

Yoshino M, Abhinav K, Yeh FC, Panesar S, Fernandes D, Pathak S, Gardner PA, Fernandez-Miranda JC, 2016. Visualization of Cranial Nerves Using High-Definition Fiber Tractography. Neurosurgery79, 146–165. [PubMed: 27070917]

Zemmoura I, Serres B, Andersson F, Barantin L, Tauber C, Filipiak I, Cottier JP, Venturini G, Destrieux C, 2014. FIBRASCAN: a novel method for 3D white matter tract reconstruction in MR space from cadaveric dissection. Neuroimage103, 106–118. [PubMed: 25234114]

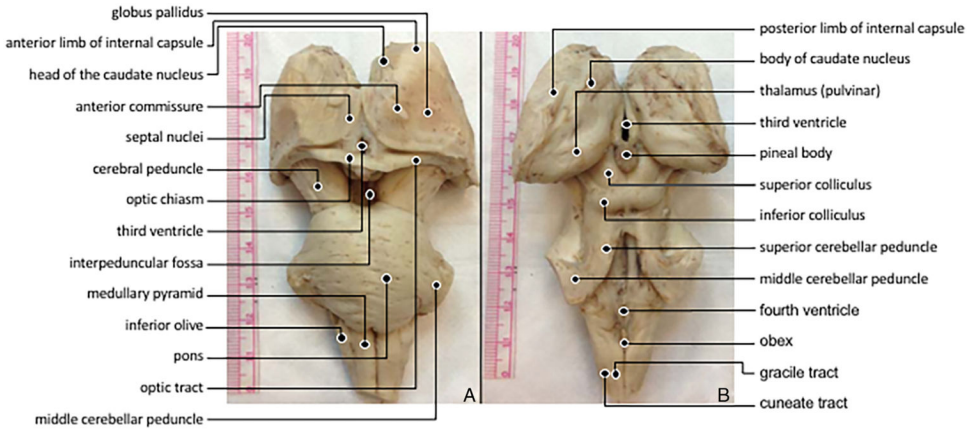

Fig. 1.

Postmortem specimen including the full brainstem and partial volumes of the medial, deep forebrain used for magnetic resonance histology. (A) ventral view. (B) dorsal view. Photographs were taken after dissection, vascular flushing and tissue fixation.

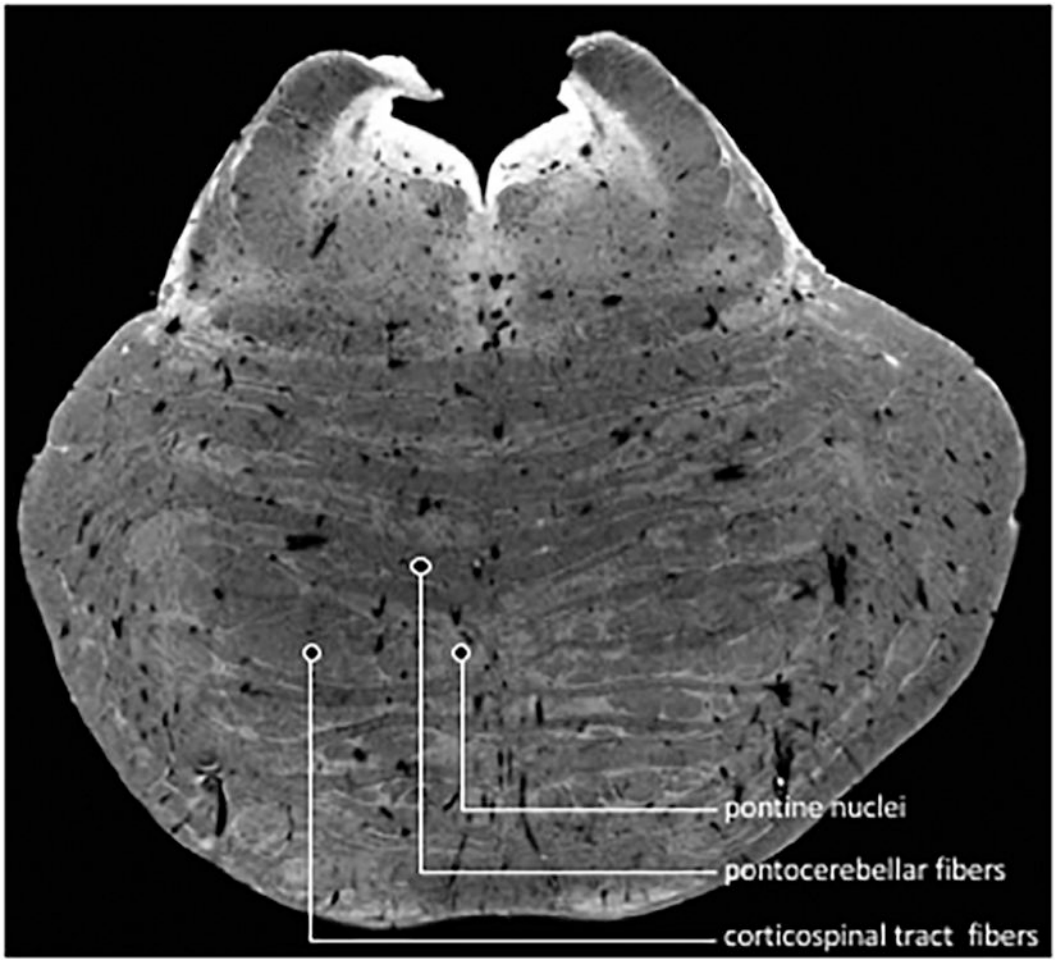

Fig. 2.

Axial GRE image slice of the brainstem at the level of the rostral pons obtained in a transverse plane, with respect to the longitudinal axis of the brainstem. The image is oriented to be consistent with most conventional histological atlases of the brainstem where ventral is toward bottom of image (inverted with respect to *in vivo* MR imaging in the axial plane). Note the visibility of descending fiber bundles of the corticospinal tracts amidst the nuclei and transverse fibers of the basilar pons.

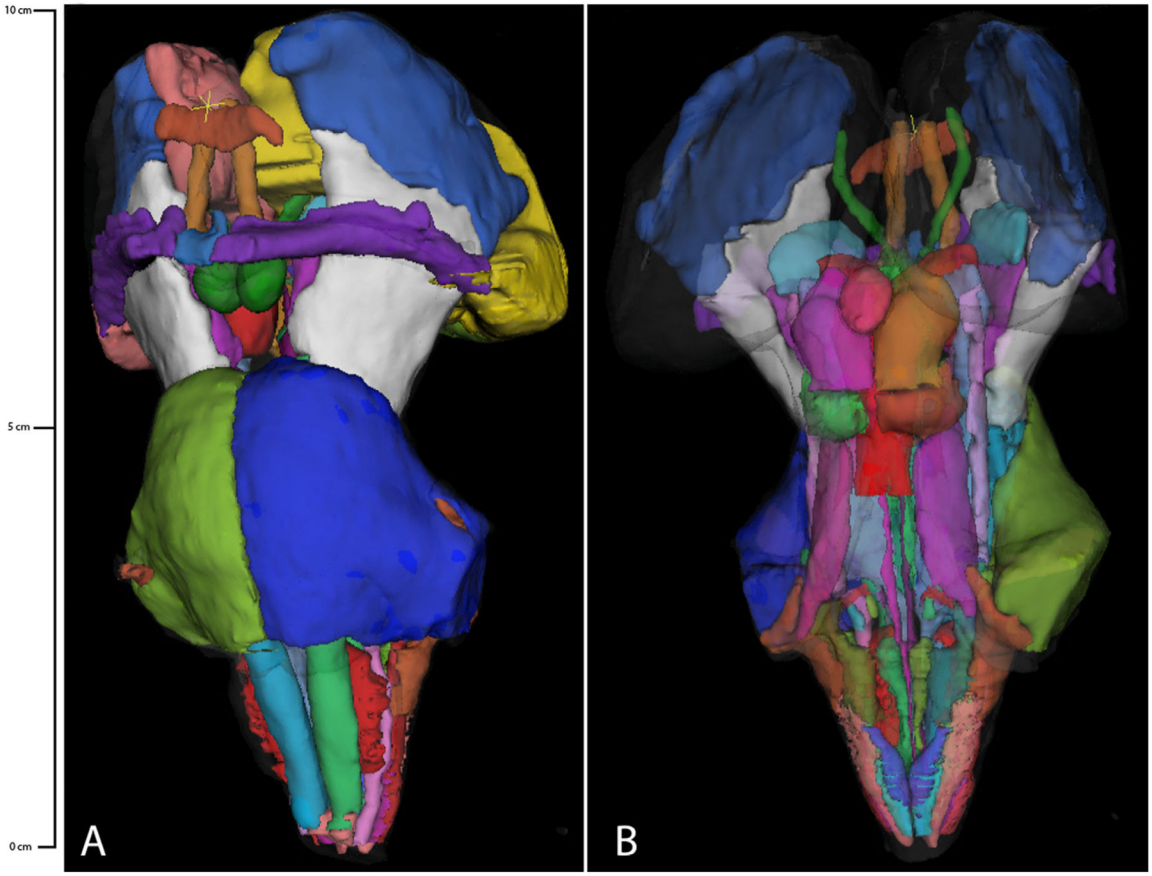

Fig. 3.

3D-rendered segmentation model used to guide tractography. Each color represents a different gray or white matter structure that could be used as a seed region or ROI for diffusion tractography. (A) Anterior surface view. (B) Posterior surface view with opacity reduced and thalamus and fourth ventricle removed for greater visibility of underlying structures.

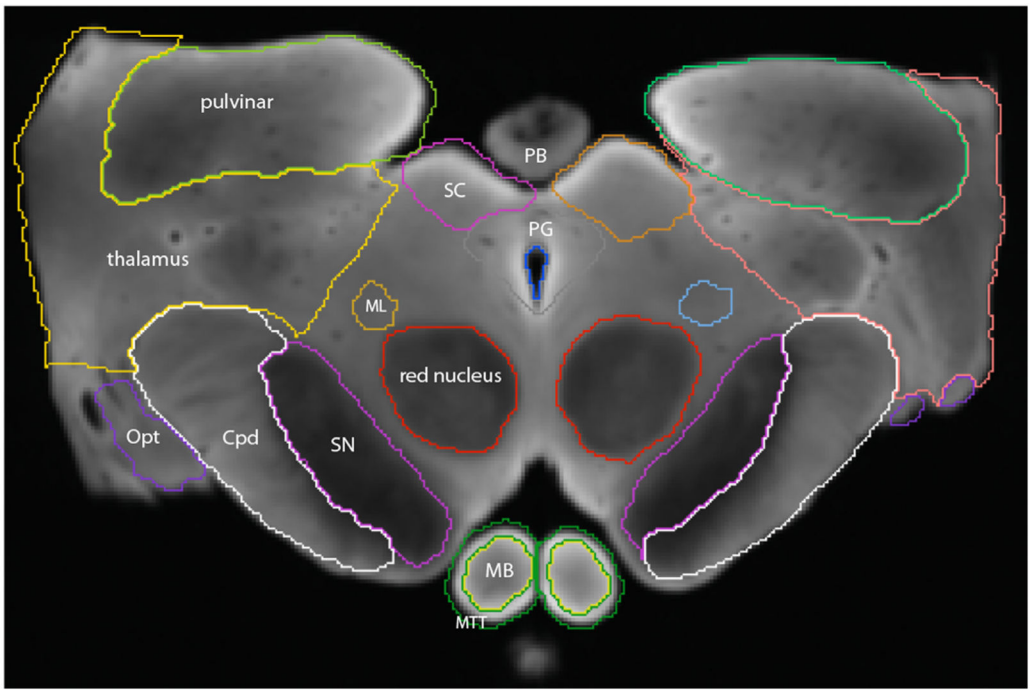

Fig. 4.

DWI image at the level of the mesencephalon demonstrating segmentation of various gray and white matter structures; image plane and orientation as in Fig. 2. Cpd, cerebral peduncle; MB, mamillary body; ML, medial lemniscus; MTT, mammillothalamic tract; Opt, optic tract; PB, pineal body; PG, periaqueductal gray; SC, superior colliculus; SN, substantia nigra.

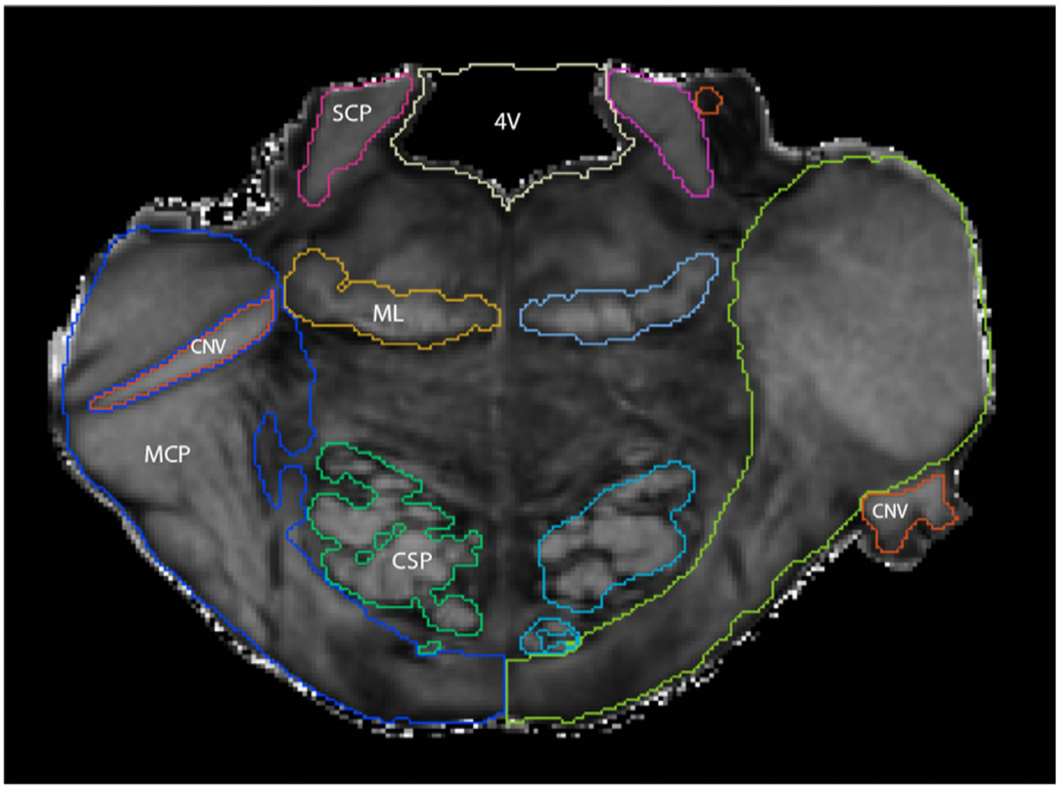

Fig. 5.

FA image from the mid-pons at the level of the root of the trigeminal nerve; image plane and orientation as in Fig. 2. FA images are useful for visualizing white matter tracts such as the cerebellar peduncles, cranial nerve roots, and major longitudinal white matter tracts of the brainstem. 4 V, fourth ventricle; CNV, cranial nerve 5; CSP, corticospinal tract; MCP, middle cerebellar peduncle; ML, medial lemniscus.

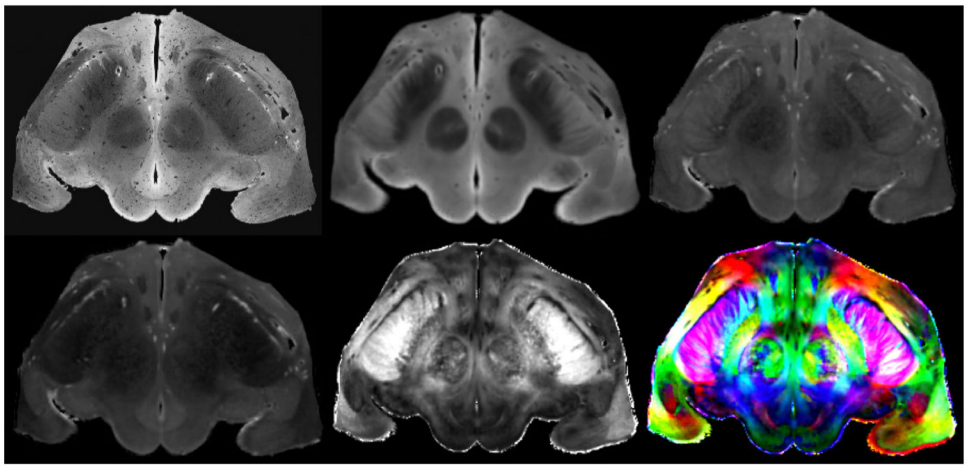

Fig. 6.

Multiple image contrasts obtained by magnetic resonance histology of a postmortem human brainstem at the level of the rostral midbrain; image plane as in Fig. 2. (A) GRE, (B) DWI, (C) AD, (D) RD, (E) FA, (F) color FA.

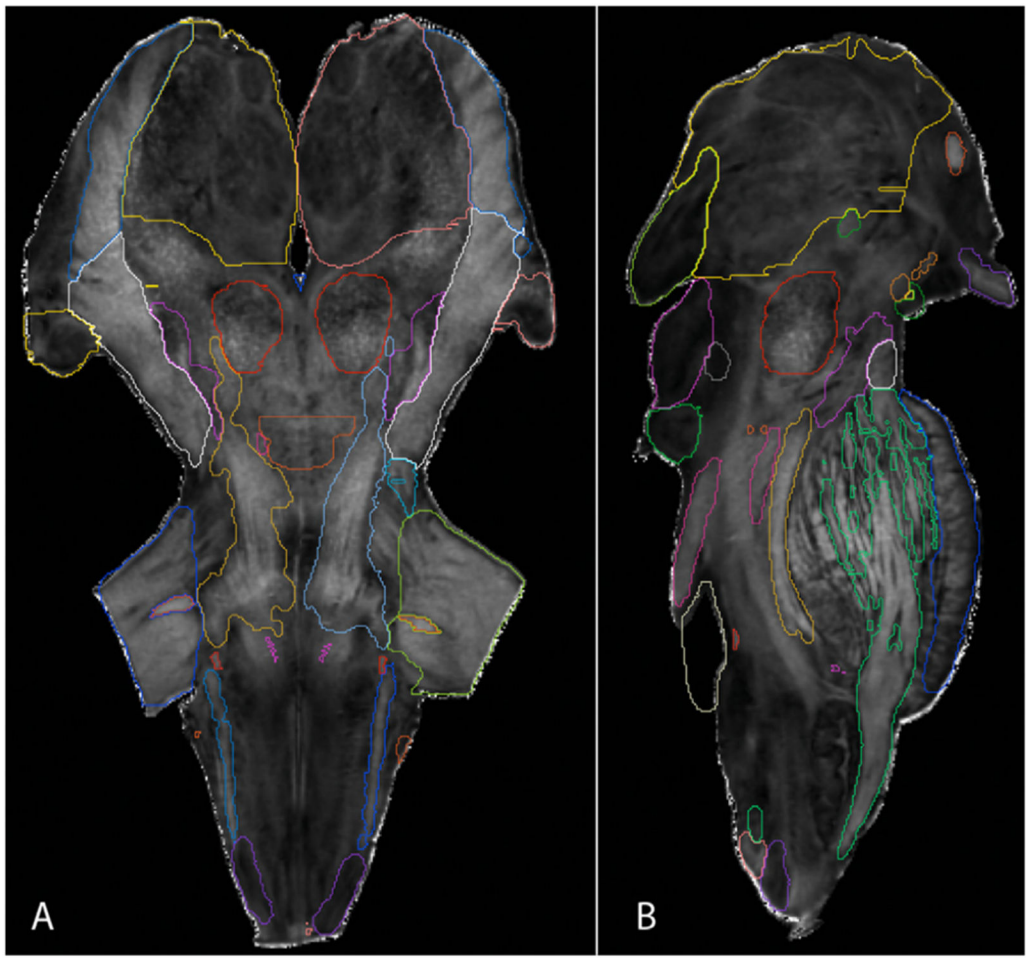

Fig. 7.

Human brainstem viewed in custom-specified longitudinal planes through the FA dataset. (A) An oblique longitudinal plane acquired by rotating approximately 60° clockwise from the axial plane. (B) Parasagittal plane. Custom planes such as these were used to more fully visualize and segment the brainstem. Delineations made in one plane transposed to any other plane.

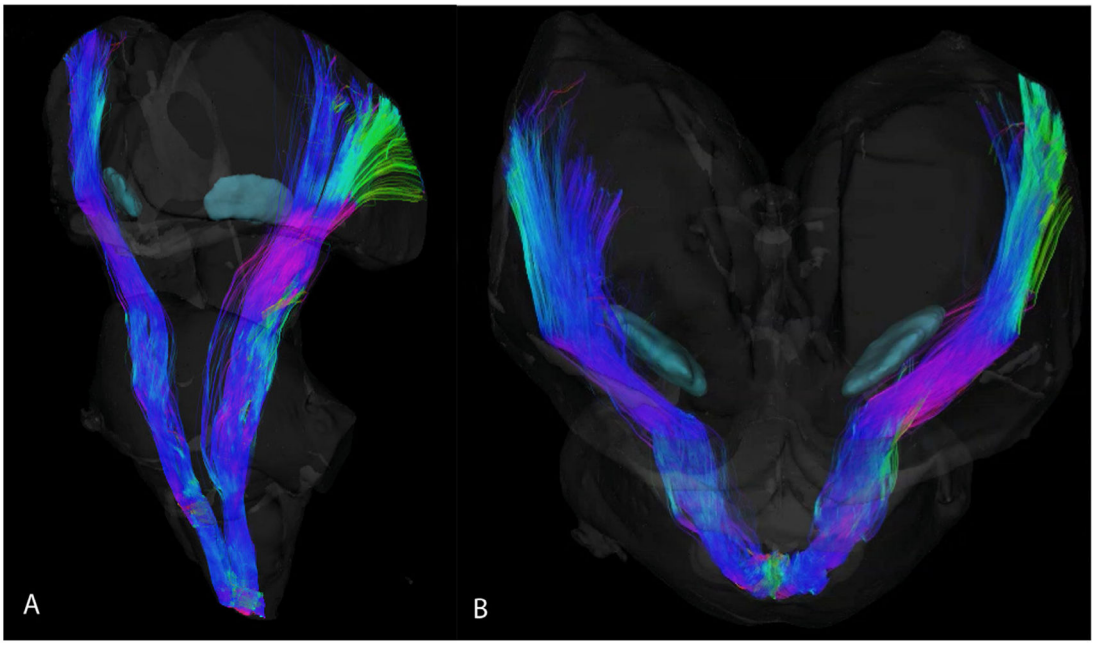

Fig. 8.

Simultaneous visualization of selected nuclei and white matter pathways. Deep brain stimulation for Parkinson's disease patients targets the subthalamic nuclei (blue) but should avoid the corticospinal tracts (fibers). Note the decussation of the corticospinal tract at the inferior end of the brainstem specimen.

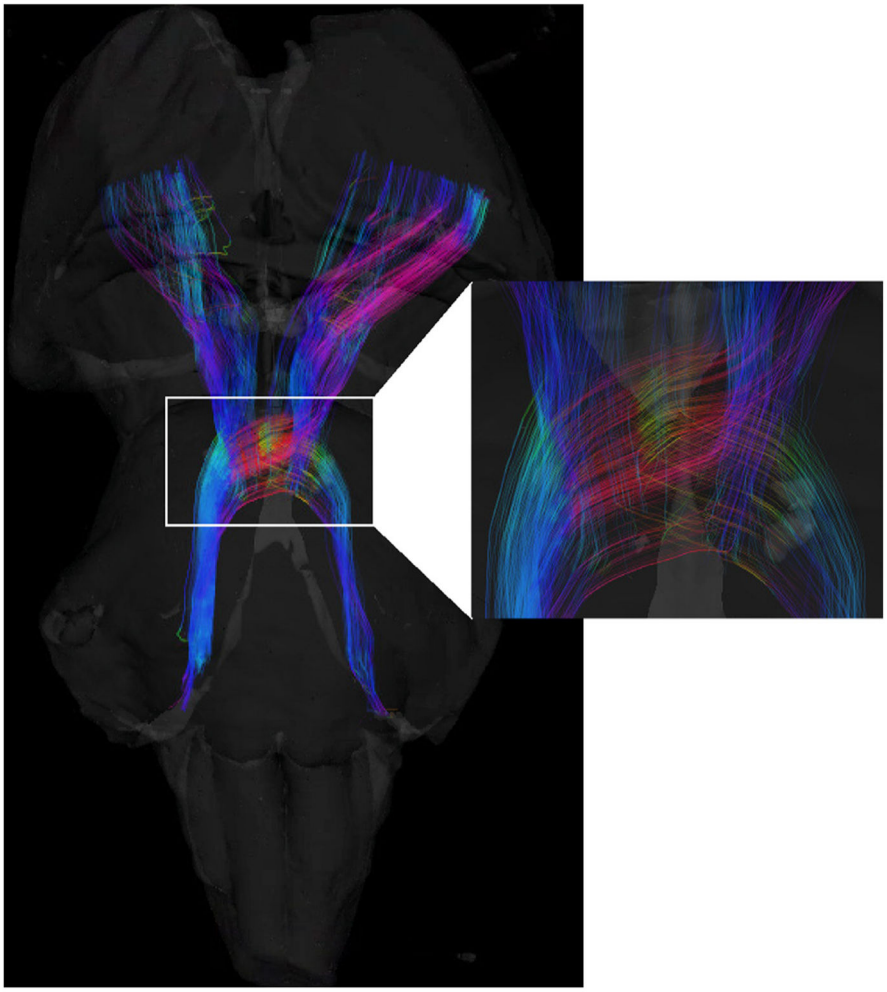

Fig. 9.

Crossing fibers in the decussation of the superior cerebellar peduncle are resolved, given the high angular resolution of imaging for magnetic resonance histology. Inset shows this decussation at higher magnification.

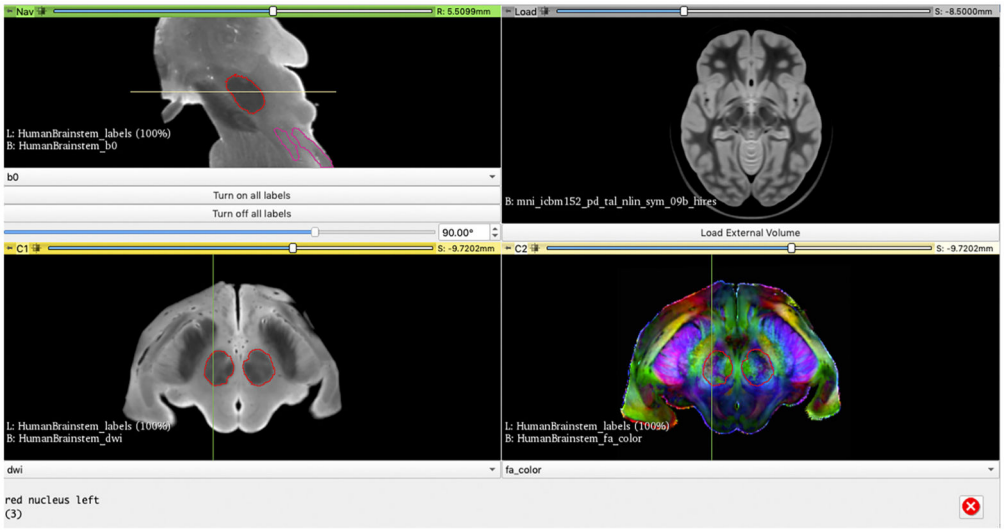

Fig. 10.

Interactive atlas viewing sections at the level of the red nucleus. Upper left shows overview of the brainstem in the midsagittal plane with interactive sliders defining location and angle of the cross-sections shown in the two lower panes. Bottom two panes show these two chosen contrasts: DWI (left) and color FA (right). The outline of the red nucleus is displayed in each of these windows. Upper right provides a pane for user to upload their own datasets or image files; the axial ICBM 152 dataset from the MNI dataset is loaded here with the level set to closely approximate the level selected for display in the lower panes.

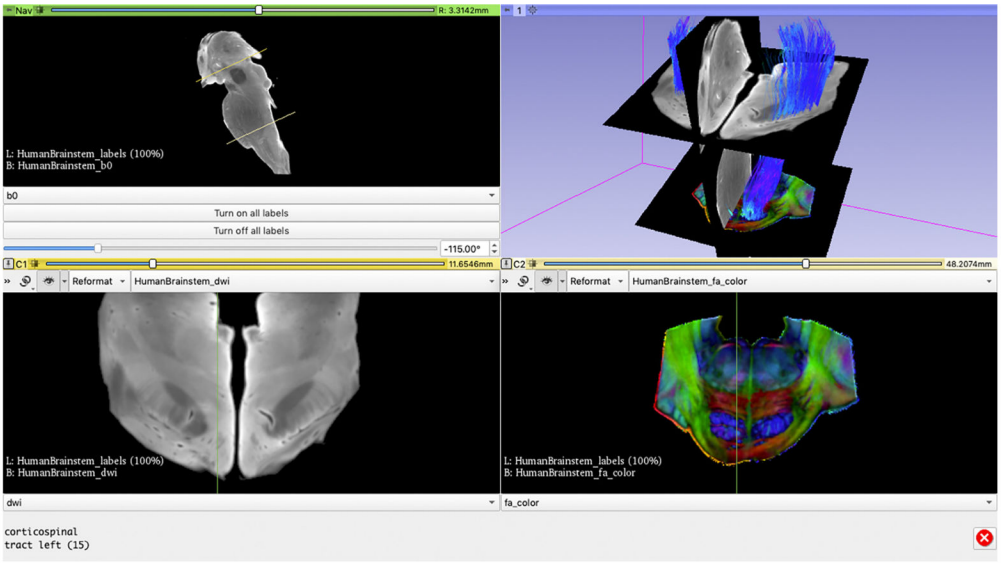

Fig. 11.

Interactive atlas viewing sections and representative DT. Upper left shows overview of the brainstem in the midsagittal plane with interactive sliders defining location and angle of the cross-sections shown in the two lower panes. Bottom two panels show two chosen contrasts at different longitudinal levels through the specimen: DWI at the level of the caudal diencephalon (left) and color FA at the level of the caudal pons (right). Upper right provides a pane for viewing in 3D a reconstructed tract derived from DT, with the sections from the other panes displayed for contextual reference. In this example, the corticospinal tracts are displayed bilaterally with the transverse sections illustrating passage of corticospinal tract fibers through the posterior limb of internal capsule into the cerebral peduncle (DWI image) and the more caudal intercalation of fibers among pontine nuclei and pontocerebellar fibers (color FA image). Users may interact with these images and tracts and vary rotational perspective, translation and magnification.

Table 1

List of all segmented structures. In total there were 90 different structures; bilateral structures are consolidated here, rendering 48 unique structures.

Gray matter	**White matter**
Diencephalon	Longitudinal tracts
Mammillary body	Corticospinal tract
Pineal gland	Medial lemniscus
Pulvinar nucleus	Medial longitudinal fasciculus
Subthalamic nucleus	Spinothalamic tract
Thalamus excluding pulvinar	
	Mesencephalon
Mesencephalon	Cerebral peduncle
Inferior colliculus	Trigeminal tract (mesencephalic)
Red nucleus	
Substantia nigra	
Superior colliculus	Metencephalon
	Inferior cerebellar peduncle
Metencephalon	Middle cerebellar peduncle
Abducens nucleus	Superior cerebellar peduncle
Facial nucleus	Superior cerebellar peduncle (decussation)
Trigeminal nucleus (motor)	
Trigeminal nucleus (principal sensory)	
	Myelencephalon
Myelencephalon	Cuneate fasciculus
Cuneate nucleus	Gracile fasciculus
Cuneate nucleus (external)	Pyramidal decussation
Gracile nucleus	Spinal trigeminal tract
Hypoglossal nucleus	
Inferior olive (principal nucleus)	Telencephalon
Spinal trigeminal nucleus (caudalis)	Anterior commissure
Spinal trigeminal nucleus (interpolaris)	Fornix (anterior columns)
	Internal capsule posterior limb
Spinal trigeminal nucleus (oralis)	Mammillothalamic tract
Vestibular nucleus	Posterior commissure
Cranial nerves	**Ventricles and spaces**
Optic chiasm	Cerebral aqueduct
Optic tract	Fourth ventricle
Roots of the abducens nerve	Obex
Roots of the facial nerve	
Roots of the trigeminal nerve	

Table 2

List of all tracts, the parameters used to generate them, and brief associated clinical relevancies.

Tract Name	ROIs or Seed Regions	# of Tracts Generated Before Refinement	Anatomical Pathway/ Main Functions	Clinical Significance
Anterior commissure (AC)	seed sphere on one end, ROI sphere on other end; reverse and repeat	50,000 (x2)	Inter-hemispheric pathway for basal frontal lobe and anterior-medial temporal lobe	creates reference plane with posterior commissure
Corticospinal tracts (CSP)	seed pyramidal decussation	20,000 (rk4)	Conveys motor commands from motor cortex to spinal cord	Avoid in STN deep brain stimulation (gives unwanted motor movement)
Dentatorubrothalamic tracts (DRT) (subset of superior cerebellar peduncles, SCP)	seed/ROI SCP, ROI contralateral red nucleus, ROI contralateral thalamus	seed SCP: 20,000; ROI SCP: 4300	Efferent pathway for ascending signals from dentate nucleus of cerebellum to mesencephalon and diencephalon	Target in ET DBS
Facial nerve roots	seed sphere on dorsal end, ROI sphere on ventral end	25,000	Motor function of facial muscles; special sensory function from anterior tongue; parasympathetic outflow for lacrimal and salivatory gland function	Avoid in surgery (facial paralysis may result if hit)
Fornix, anterior columns	seed sphere on caudal end, ROI sphere on rostral end	25,000	Major tract of hippocampus connecting hippocampal structures to preoptic and posterior diencephalic nuclei; role in memory	Potential DBS target in Alzheimer's Disease
Inferior cerebellar peduncles (ICP) & Dorsal columns (DC)	ROI ICP	5000	ICP connects spinal cord and medulla to cerebellum; DCs convey mechanosensory information from the postcranial body to the brainstem	DC stimulation used to treat chronic neuropathic pain
Mammillothalamic tracts (MT)	seed MT, ROI thalamus	20,000	Projections from the mammillary bodies to the anterior nucleus of the thalamus	Target in epilepsy DBS
Medial lemnisci (ML)	seed ML	right: 10,000; left: 20,000 (rk4)	Carries tactile and proprioceptive information from DC nuclei to VPL nucleus of thalamus	Avoid in DRT DBS (loss of proprioception)
Optic tracts	ROI optic chiasm	5000	Axons of retinal ganglion cells caudal to optic chiasm projecting to targets in diencephalon and mesencephalon	Transmit visual information to thalamus (thus typically avoid)
Posterior commissure (PC)	ROI circle on one end, ROI circle on other end; large ROA through pons	8500	Inter-hemisphere pathway for pretectum and rostral mesenecephalon; crosses midline just dorsal to cerebral aqueduct	Pupillary light reflex; creates reference plane with anterior commissure
Trigeminal nerve roots (TN) & Spinal trigeminal tracts (STT)	seed TN, ROI STT	25,000	TN: Penetrates pontocerebellar fibers in the lateral pons; somatic sensation for face; motor innervate muscles of mastication STT: axons carrying nociceptive/thermal signals, formed from first order trigeminal ganglion neurons extending from midpons through caudal medulla	Modulate mechanism of NC DREZ surgery

Abbreviations: ET (Essential Tremor), DBS (deep brain stimulation), NC DREZ (nucleus caudalis dorsal root entry zone), STN (subthalamic nucleus), ROA (region of avoidance), ROI (region of interest), VPL (ventral posterior lateral).